Compression behaviour of bulk nanocrystalline Ni-Fe

2002 J. Phys.: Condens. Matter 14 2605

(http://iopscience.iop.org/0953-8984/14/10/311)

INSTITUTE OF PHYSICS PUBLISHING JOURNAL OF PHYSICS: CONDENSED MATTER

J. Phys.: Condens. Matter **14** (2002) 2605–2620 PII: S0953-8984(02)30218-2

Compression behaviour of bulk nanocrystalline Ni–Fe

X Y Qin[1], X G Zhu[1], S Gao[2], L F Chi[2] and J S Lee[3]

[1] Key Laboratory of Internal Friction and Defects in Solids, Institute of Solid State Physics, Academia Sinica, 230031 Hefei, People's Republic of China
[2] Physikalishes Institut, Universitaet Muenster, Wilhelm-Klemm Strasse 10, D-48149, Muenster, Germany
[3] Department of Metallurgy and Material Science, Hanyang University, 425-791 Ansan, Korea

Received 18 October 2001, in final form 15 January 2002
Published 18 March 2002
Online at stacks.iop.org/JPhysCM/14/2605

Abstract

The mechanical behaviour of fully dense nanocrystalline Ni–19Fe (grain size 36–37 nm) was investigated by compression and deformation-trace observations with optical microscopy and atomic force microscopy in the temperature range from −162 to 600 °C. The results indicated that yield stress ($\sigma_{0.2}$) increased with increasing strain rate with strain-rate sensitivity exponent $m = 0.01$ at ambient temperature. At the temperatures $T < 100\,^{\circ}\mathrm{C}$ or $T > 400\,^{\circ}\mathrm{C}$ yield strength decreased gradually with increasing temperature, while it dropped catastrophically in the range $100\,^{\circ}\mathrm{C} < T < 400\,^{\circ}\mathrm{C}$. Low-temperature deformation produced two sets of macroscopic bandlike traces which oriented at around 55° to the compression axis and consisted of ultra-fine straight lines; in contrast, high-temperature deformation led to formation of microcavities accompanying which some nanograins arranged locally in regular form. The results on both mechanical behaviour and deformation morphology suggest that the deformation mechanism at low temperatures was different from that at high temperatures, with the transition temperature locating at $T_c \sim 340\,^{\circ}\mathrm{C}$.

(Some figures in this article are in colour only in the electronic version)

1. Introduction

Nanocrystalline materials (n-materials), i.e. polycrystalline materials with grain size less than 100 nm, are of considerable scientific and technological interests at present [1, 2]. Since the early days of research in this field, mechanical properties of n-materials have aroused much attention due to their extremely fine grain sizes and large volume fraction (5–50%) of interfaces, which may lead to different and/or improved mechanical properties, such as high strength in n-metals [3] and high ductility in n-ceramics [4]. In the meantime, some conflicting results in the mechanical behaviour have been reported. For instance, some investigators reported that the normal Hall–Petch (HP) relation existed [5–9], while

others reported that inverse HP relations (hardness decreased with decreasing grain size) were found in some n-materials [10–12]. Even hardening and softening behaviour on decreasing grain size were found to co-exist in some n-materials [13–15]. In recent work, the relationship between Vickers hardness and yield stress in n-Cu were found to be different from that in conventional polycrystalline materials [16]. Although there have been some attempts [17, 18] to reveal the intrinsic mechanical behaviour and plastic deformation mechanisms in n-materials, little, if any, understanding exist, especially for the n-materials with grain size <50 nm. In view of most work conducted early (for early work see e.g. [15]), we believe that one of the main reasons for conflicting results and uncertainty (see e.g. [5, 13, 19, 20]) in experimental phenomena and lack of understanding of deformation mechanism lie in difficulties in manufacturing large, dense and (geometrically) standard specimens for conventional mechanical tests, which limited the utilization of conventional test and analysis methods. Hence, in order to extract intrinsic mechanical behaviour and acquire deformation mechanisms of n-materials it is significant for one to prepare (nearly) full dense n-material and to perform mechanical tests with conventional test methods on standard specimens.

In this paper, we report our investigations on compressive mechanical behaviour of bulk nanocrystalline γ-Ni–xFe(n-Ni–Fe) with $x = 19.4$ wt%, synthesized by a mechano-chemical process plus hot isostatic pressing (HIPing). γ-Ni–xFe with $x = 10$–65 wt%, so-called permalloy, are important materials with wide applications in industry [21]. Many techniques [14,22–26] have been utilized to prepare n-Ni–Fe, mostly in powder state. However, mechanical properties of bulk n-Ni–Fe with nearly full density were rarely reported except harness tests [14]. The synthetic method used here has been shown [26] to be an effective one that has the advantage of producing nanopowders with large quantity and light agglomeration, while HIPing [27] is one of the effective routes for consolidating powder into bulk material at relatively low temperatures and in a short time, being beneficial to retaining nanophase microstuructures. The mechanical properties of n-Ni–Fe were tested by conventional compression, while optical microscopy (OM) and atomic force microscopy (AFM) were utilized to reveal deformation characteristics (morphology) on elaborated specimen surfaces. Emphasis was laid on combination of mechanical behaviour with deformation morphology to analyse the deformation mechanism.

2. Experiment

2.1. Synthesis of n-Ni–Fe bulk material

The powders of n-Ni–Fe alloy were synthesized by using a mechano-chemical process [26,28]. Briefly, first the dry mixed oxide powder was obtained by blending α-Fe_2O_3 (30 μm, 99.99%) and NiO (4 μm, 99.99%). Then these dry mixed oxides were ball milled in methyl alcohol at a speed of 300 rpm for 10 h. The ball media and impeller used were made of stainless steel. After ball milling they were dried and sieved. The milled oxides were then reduced at 500 °C for 1 h and consecutively at 550 °C for *in situ* alloying for 0.5 h in hydrogen so as to form γ-Ni–Fe alloy powder.

The obtained Ni–Fe powders (with grain size ∼20 nm) were then compacted, under uni-axial pressure of ∼900 MPa, into rectangular-shaped raw bars with density of 60–65%. The raw bars were then pre-sintered at 650 °C for 1.5 h in hydrogen flow to remove any residual oxides and to protect them from oxidation. High-density bars were prepared by using HIPing at Bodycote IMT GmbH, Essen, Germany. To do this, the pre-sintered bars were embedded in high-purity Al_2O_3 powder that was sealed in an evacuated stainless can, and then isostatically pressed at 750 °C for 1 h under 190 MPa in Ar atmosphere.

2.2. Processing of specimens for mechanical testing and surface observation

Strip-shaped specimens were cut from HIPed bars with a spark erosion machine. To avoid the effect of surface damage by spark erosion and to reduce surface flaws, a layer of more than $\sim$0.1 mm in thickness was polished away from all sides of the as-machined specimens first with grinding papers (the final one was No 800 paper) and then with diamond pastes (the final one with a particle size of 1 μm). Specimen length was always three times greater than the largest lateral dimension (typical size was $\sim 6.2 \times (\sim 2) \times (\sim 2)$ mm^3 after polishing). To observe deformation traces with OM and AFM, one lateral surface for each specimen was further specially polished using diamond paste of particle size 1/4 μm. In the polishing process, we always checked the polishing quality by observations with OM under magnification of $\times$500 until no obvious scratches were observable. Then they were etched with Nital (3% HNO_3 + 97% alcohol) for 15 s. There was no surface preparation after deformation.

2.3. Microstructural characterization

The crystalline structure and mean grain size (based on the Scherrer formula) of the material were checked using x-ray diffraction (XRD) with Cu Kα radiation, where the instrumental broadening was calibrated with an annealed Si standard. Main chemical components and minor compositions were determined by energy dispersive x-ray spectroscopy (EDS) and emission spectrum (ES), respectively. The specimen densities were measured based on Archimedes' principle with an accuracy of $\pm$0.2%. Both OM and AFM were used to observe the polished specimen surfaces before and after compression to reveal deformation traces.

2.4. Mechanical tests

The compression tests were carried out on an Instron machine (model 1195). For low-temperature tests a cryostat was set up, which was filled with liquid nitrogen automatically and controlled by a computer. For high-temperature experiments the machine was equipped with a furnace in which a quartz tube was mounted. High-purity (99.999%) argon flow was introduced into the tube during experiments to avoid specimen oxidation. Two well machined hard-metal plates were placed in between specimen ends and the anvil heads. MoS_2 powder was sprayed on the plates for lubrication. Normally, an initial strain rate of $\sim 1.4 \times 10^{-4}$ s^{-1} was used. For investigation of strain rate sensitivity, strain rate was changed from 1.4×10^{-5} to 5.6×10^{-1}s^{-1}.

3. Results

3.1. Microstructural characterization

Figure 1 gives a typical XRD pattern for n-Ni–Fe after HIPing, where the XRD pattern for pure Ni is also given for the sake of comparison. By comparing the two curves, one can deduce that the obtained Ni–Fe alloy has fcc crystal structure (γ phase), the same as that of Ni. However, there was broadening for each peak in curve (b) as compared with (a), which indicates the grain refinement for the obtained Ni–Fe alloy. The mean grain sizes were determined from XRD to be around 36–37 nm as given in table 1. Grain size and morphology was also observed using AFM. As an example, figure 2 shows a typical AFM image observed on the specimen surface before deformation. It can be seen from this figure that the grains are arranged randomly with fairly homogeneous sizes, and largely display spherical shape. Most of the grains had a size of about 40 nm, which agreed with XRD results.

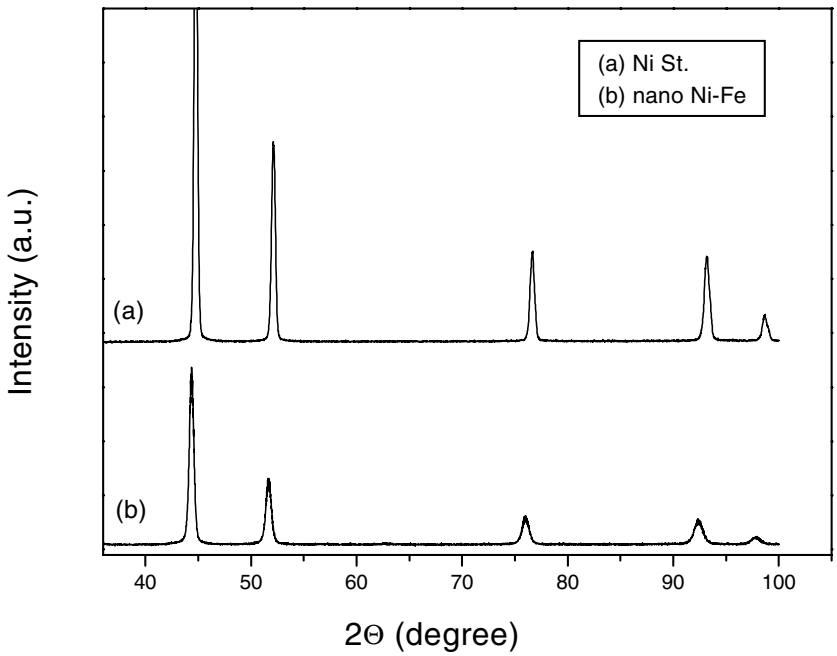

Figure 1. XRD patterns (Cu Kα radiation) for (*a*) a nickel standard and (*b*) n-Ni–Fe.

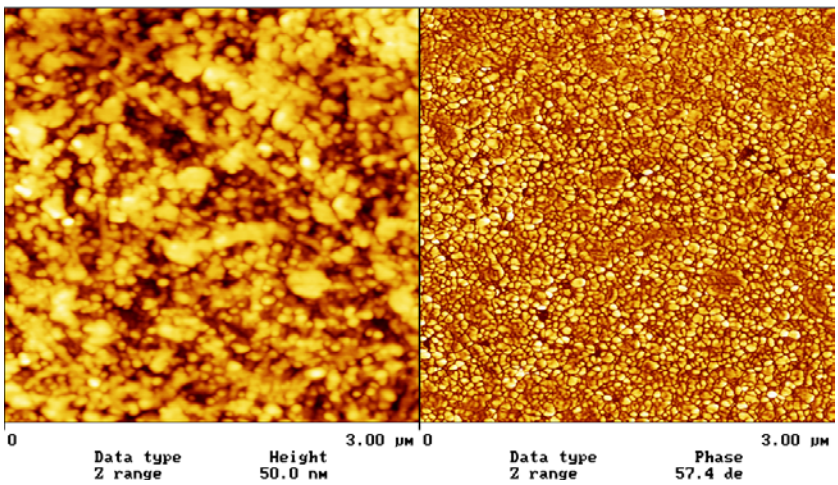

Figure 2. AFM images (image size 3 μm $\times$ 3 μm) for a specimen surface before compression. Left, height image; right, phase image (this shows the same viewing field as on the left).

Table 1 lists the analytical results of chemical composition for two HIPed bars used here. It can be seen that the concentrations for Ni and Fe were around 80 and $\sim$19 wt%, respectively. Apart from the main components (Ni, Fe), there were impurity elements Cr, Mn, Al and Si existing in the bulk material. The Cr content was $\sim$0.1%, and the contents for other elements were $\leqslant$0.05 wt%. The densities of the HIPed bars were determined to be $\sim$8.5 g cm^{-3} as shown in table 1. Assuming the theoretical density ρ_0 for n-Ni–Fe is the

Table 1. A list of mean grain size d, density ρ, fraction density D_r and compositions of two n-Ni–Fe bars after HIPing at 750 °C for 1 h.

				Composition (wt%)					
Bar	d (nm)	ρ (g cm^{-3})	D_r (%)	Ni	Fe	Cr	Mn	Al	Si
S1	36 ± 3	8.49 ± 0.02	98.5	80.4 ± 0.5	19.4 ± 0.5	0.10 ± 0.05	0.05 ± 0.01	0.03 ± 0.01	0.05 ± 0.02
S2	37 ± 3	8.49 ± 0.02	98.5	80.3 ± 0.5	19.4 ± 0.5	0.15 ± 0.05	0.05 ± 0.01	0.05 ± 0.01	0.05 ± 0.02

same as that (8.62 g cm^{-3}) [21] of conventional Ni–Fe with the same Ni content, the fraction density for both bars was 98.5% as listed in table 1. It can be seen from table 1 that the grain sizes, densification and chemical compositions for the two bars had no obvious difference. However, for the sake of consistency of the data and reducing experimental errors caused by microstructural differences, in the following mechanical experiments a series of specimens cut from S1 were used for investigations of strain rate effect. The other series of specimens cut from S2 were used to explore temperature effects on mechanical behaviour.

3.2. The effect of strain rate on yield strength

To explore the effect of strain rate on yield strength, a series of specimens cut from S1 were compressed at room temperature. Figure 3 shows engineering strain–stress curves obtained at three different strain rates. It can be seen from this figure that plastic deformation occurred at the stress level of about 1.5–1.6 GPa for all the specimens tested. After plastically deforming to a strain of about 0.5%, the stress decreased with further deformation. After compression tests stopped, we found that bending occurred for all the specimens. Therefore, the decrease in flow stress after further deformation was caused by bending of the specimens. Furthermore, it can be roughly seen from figure 3 that the material becomes harder with increasing strain rate as one compares curve (a) with (b) and (c). Figure 4 gives yield strength ($\sigma_{0.2}$) as a function of strain rate. It can be seen from this figure that yield strength rose rapidly from 1.54 to about 1.61 GPa when strain rate increased from 1.39×10^{-5} to 1.39×10^{-3} s^{-1}. As strain rate increased further, the increase in yield stress became slower. The strain rate sensitivity exponent (SRSE), m, according to formula

$$\sigma_{0.2} = B\dot{\varepsilon}^m \tag{1}$$

can be obtained by determining the slope in a plot $\ln \sigma_{0.2}$ versus $\ln \dot{\varepsilon}$. Here $\dot{\varepsilon}$ is strain rate, and B is a constant. Figure 5 shows this plot. By best fit of the data, one obtains the exponent $m = 0.01 \pm 0.001$ and the factor $B = 1.73 \pm 0.02$ (GPa). This result indicates that strain rate has an obvious influence on the yield strength for n-Ni–Fe in the whole strain range investigated.

3.3. The effect of deformation temperature on yield strength

In order to examine the temperature effect on the mechanical behaviour, compression tests were conducted in the temperature range from −162 to 600 °C at a constant strain rate of 1.39×10^{-4} s^{-1}. The yield strength for a series of specimens cut from S2 is given in figure 6 as a function of temperature. It can be seen from this figure that yield strength decreased gradually from 1.8 to about 1.6 GPa as temperature increased from −162 to 100 °C; then it decreased rapidly from 1.6 to 0.15 GPa as temperature increased from 100 to 500 °C. As the temperature increased further, the decrease in yield strength became slow again. The characteristic temperature at which the yield stress dropped at the fastest rate can be determined

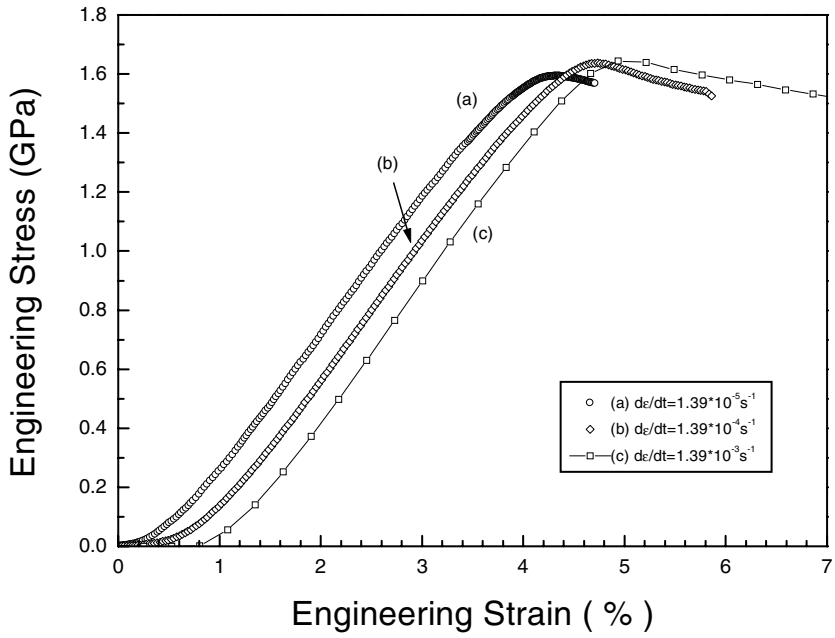

Figure 3. Engineering stress–strain curves obtained at strain rate (a) 1.39×10^{-5} s^{-1}, (b) 1.39×10^{-4} s^{-1} and (c) 1.39×10^{-3} s^{-1}.

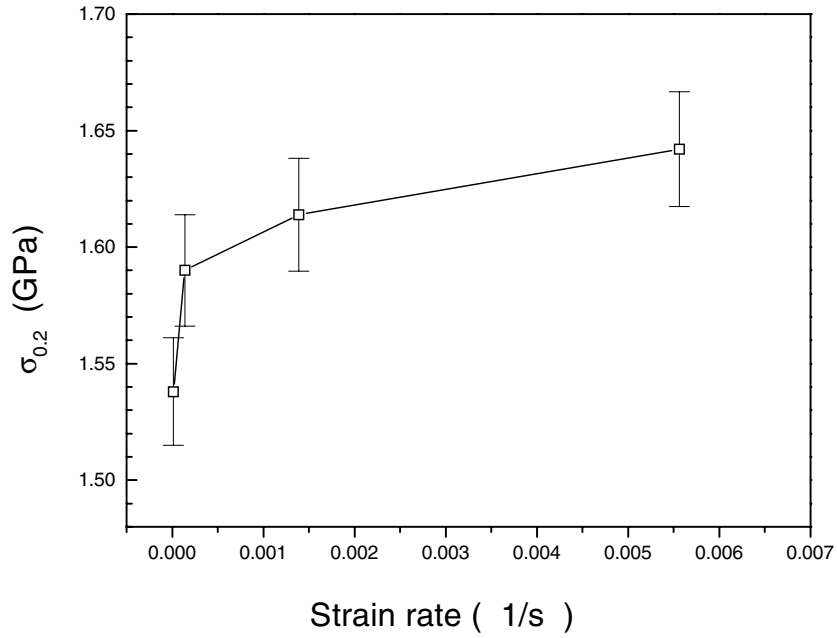

Figure 4. Variation of the yield stress with strain rate.

by differentiating yield strength with respect to temperature, which gives $T_c \approx 340\,^{\circ}$C, as shown in the inset of figure 6.

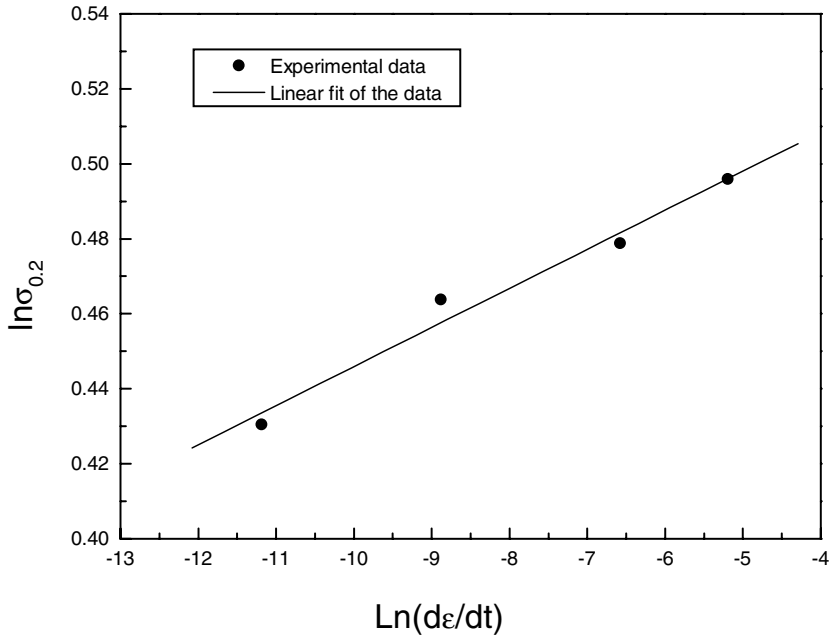

Figure 5. The plot of $\ln \sigma_{0.2}$ versus $\ln \dot{\varepsilon}$. Solid circles are experiment data, and the straight line is the best linear fit to the data.

3.4. Observations on deformation morphology

3.4.1. Deformation at room or low temperatures. Figure 7(*a*) gives a typical OM micrograph (with magnification ×200) that shows the specimen-surface morphology before deformation. It can be seen that the surface is fairly smooth, no obvious scratches produced by polishing or other oriented regular markings being observable at this resolution. In contrast, after compression tests were performed (usually with nominal strain of 1–3%), OM observations indicated that a large number of regular markings appeared in the regions near both ends of the compressed specimens (figure 7(*b*)). Figure 7(*b*) is a typical OM micrograph of the surface morphology for a specimen compressed (to a nominal strain 2%) at room temperature under the strain rate of 1.39×10^{-4} s^{-1}. By comparing figure 7(*b*) with (*a*) one can conclude that the oriented regular markings in figure 7(*b*) were caused by plastic deformation, i.e. deformation traces. The striking feature of the morphology in figure 7(*b*) was the formation of two sets of macroscopic bandlike traces (BLTs) that were symmetric to the load axis and most of them oriented at around 50°–60° to the compression axis. These BLTs were more or less similar to those reported by Nieman *et al* [19], where only one set of BLTs was observed under OM (it is worthwhile to point out that these regular markings were invisible under SEM or even under field emission SEM presumably due to their gentle wavy structure, as mentioned by Nieman *et al* [19]). With increasing temperature, the area with these deformation traces in the specimen surfaces became large and extended more to the centre part.

The surface morphologies of the specimens before and after deformation were further investigated by using AFM. Figure 8(*a*) gives an AFM image for the surface topography without deformation. It can be seen that at this resolution some scratches on the surface (labelled by 's') can be observed, which oriented randomly and had cross dimension similar

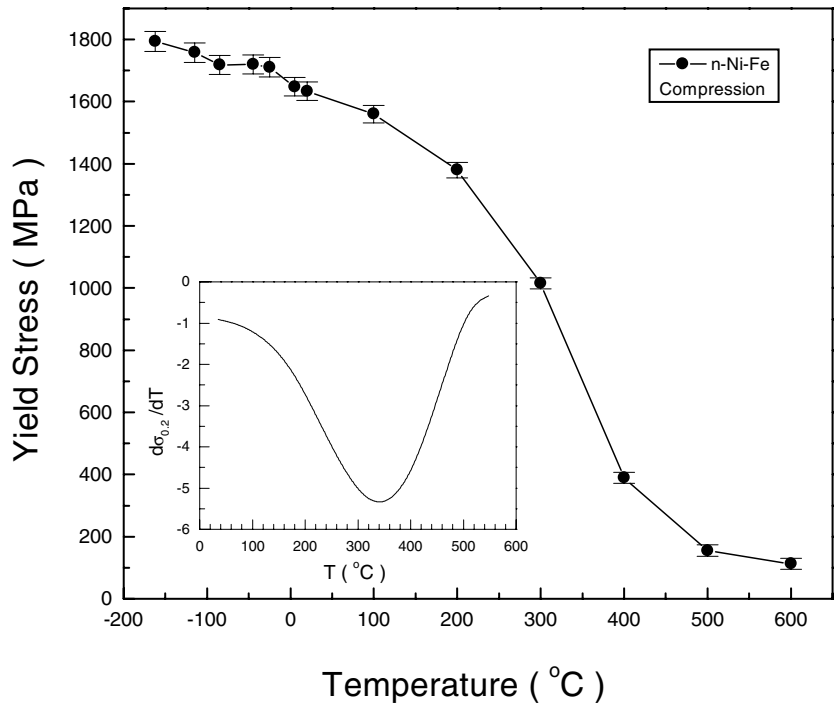

Figure 6. Yield stress ($\sigma_{0.2}$) as a function of temperature (strain rate 1.39×10^{-4} s^{-1}). The inset shows the changing rate of the yield stress ($\mathrm{d}\sigma_{0.2}/\mathrm{d}T$) with temperature.

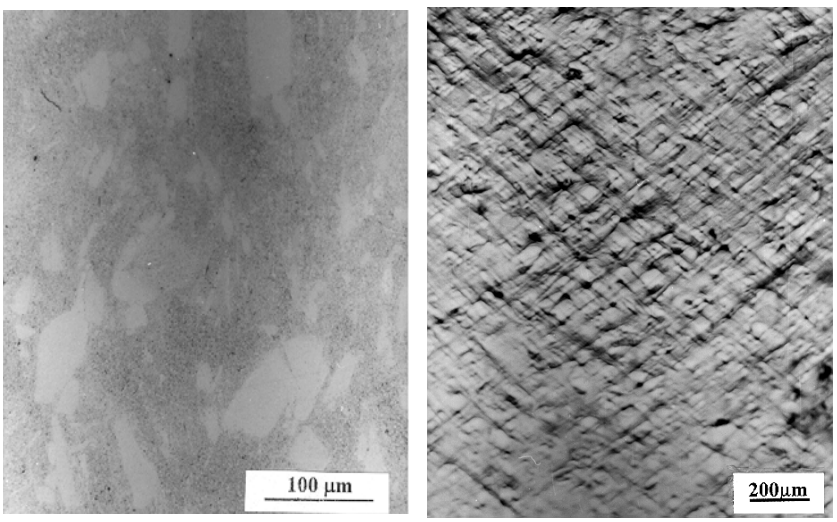

(a) (b)

Figure 7. Optical micrographs of specimen (lateral) surface morphologies (*a*) without deformation and (*b*) after compression at room temperature, where the direction of the compression axis is vertical.

to the particle size (1/4 μm) of the diamond paste used. Apart from these scratches, there was no regular band structure on the surface being resolved. In contrast to this morphology characteristic, besides some fine scratches still being visible there were two sets of regularly orienting markings appearing on the surface after deformation (figure 8(*b*)). Figure 8(*b*) is a typical AFM image for the surface morphology of the specimen after deformation (corresponding to figure 7(*b*)). By comparing figure 8(*b*) with (*a*) and 7(*b*), one can conclude that these regular markings correspond to BLTs in figure 7(*b*) and were produced by deformation. At this resolution (image size 40 μm $\times$ 40 μm), the BLTs were found to constitute parallelogramic grids on the surfaces. The statistical orientations of the two sets of the BLTs shown in figure 8(*b*) can be determined by analysing the image with fast Fourier transformation (FFT) and the result is shown in the inset of figure 8(*b*). This pattern indicated that the angle between the two sets of BLTs was $110^\circ \pm 1.5^\circ$, which means that the BLTs as a whole oriented at an angle of $\theta = 55^\circ$ to the compression axis. Figure 9(*a*) gives an AFM image of surface morphology after deformation at much higher resolution; for comparison, a typical surface morphology without deformation is also shown in figure 9(*b*), in which one can still see several fine scratches that were very shallow and distributed randomly in orientation. In contrast, on the deformed surface a large number of oriented, densely distributed regular markings (sharp lines) appeared. By comparing figure 9(*a*) with (*b*), one has reason to conclude that the regular markings in figure 9(*a*) were microscopic plastic deformation traces. In this image, grain contours are faint, but they are resolvable. Specially, one can see clearly a great number of sharp (with most of their transverse dimensions being several to dozens of nanometres) lines, more accurately nanochannels or grooves, demonstrating ultra-fine structures of BLTs (figures 7 and 8). Generally, the orientations of most of these straight nanochannels or grooves were consistent with that of macroscopic BLTs. Due to limitations of the spatial resolution ($\sim$10–15 nm) of AFM, it is difficult to resolve whether deformation happened within the individual nanograins ($\sim$30 nm). Nevertheless, by closely inspecting the image one can see that most of the sharp channels ran through in between the grains, suggesting deformation occurred mainly within grain boundary (GB) regions. Observations with OM and AFM showed that at temperatures below 300 °C the main features of deformation bands were similar to those shown in figures 7–9.

3.4.2. Deformation at high temperatures. Deformation at higher temperatures, 500 or 600 °C for instance, resulted in the deformed area being distributed homogeneously in the whole specimen. The deformation bands, although still present, were not as obvious as those appearing at lower temperatures. Figure 10 gives an AFM image (image size 40 μm $\times$ 40 μm) of the specimen surface compressed (to a strain of 2%) at 600 °C. In contrast to the bandlike feature shown in figure 8(*b*), the specimen surface appeared very smooth and even, no substantial relief structure being resolved. However, the surface displayed porous structure. This feature, as shown more clearly in figure 11 with higher resolution, turns out to be microcavities formed during deformation. Furthermore, accompanying formation of these microcavities a great number of nanograins (with sizes similar to those as shown in figure 2) aligned in a sub-micrometre scale (figure 11(*b*)). Specially, some nanograins arranged in twisted states locally, forming large particulates, such as that shown by an arrow in figure 11(*a*). Nevertheless, the large particulates with sub-micrometre size shown in figure 11(*a*) were actually assemblies as revealed in figure 11(*b*), which means that the nanograins did not merge together by grain growth, for one can still distinguish granular structure within the large aggregates from figure 11(*b*).

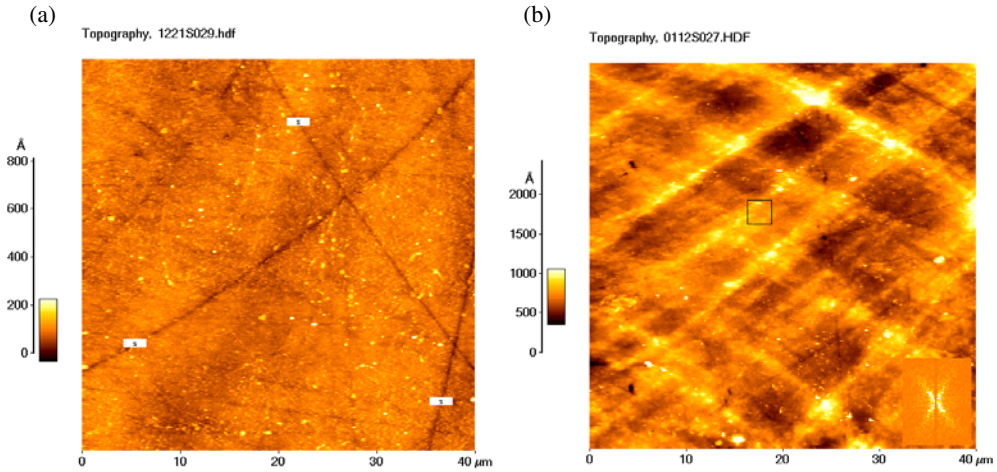

Figure 8. Typical AFM images (image size 40 μm × 40 μm) of the specimen surface morphologies (*a*) without deformation and (*b*) after deformation, where the direction of the compression axis is vertical, and the inset in the right corner shows the analytical result of FFT for the image.

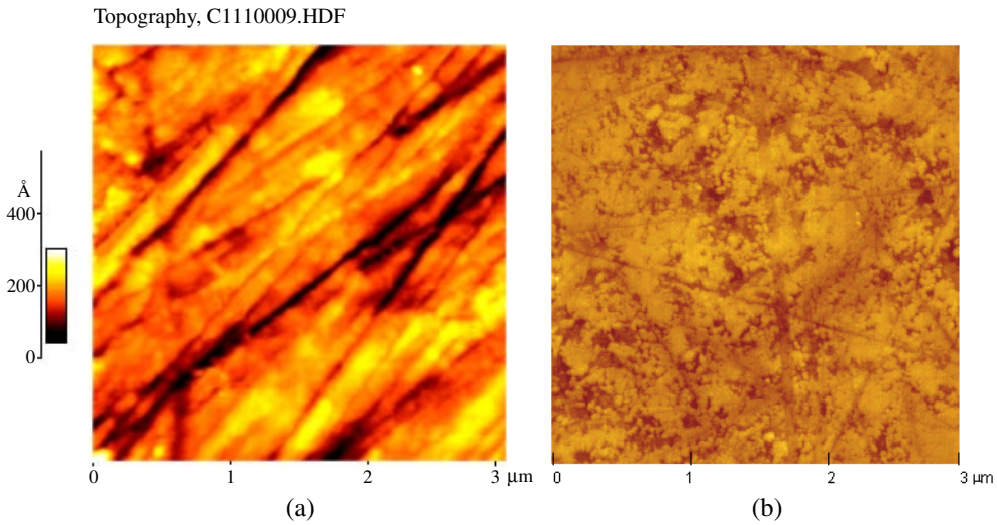

Figure 9. AFM images with high resolution (image size 3 μm × 3 μm) for the surface morphologies (*a*) after deformation—the viewing field is shown by the square in figure 8(*b*) (the direction of the compression axis is vertical)—and (*b*) without deformation.

4. Discussions

4.1. Deformation mechanism at low temperatures

At room or low temperatures, the n-Ni–Fe specimens showed very high strength with yield strength $\sigma_{0.2} > \sim$1.6 GPa (figure 6). This value of yield strength is more than ten times the literature values (150 MPa) for the permalloy with similar Ni content [29], and even greater than that ($\sim$1.4 GPa) of high-strength steels [30]. This poses a basic question, i.e. what is the deformation mechanism for n-Ni–Fe at low temperatures? Deformation morphology

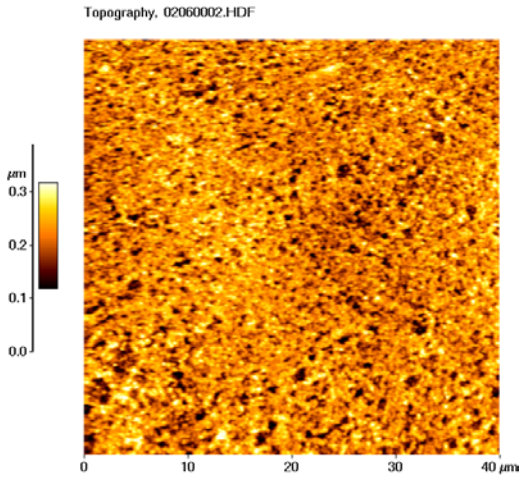

Figure 10. An AFM image (image size 40 μm × 40 μm) of a lateral specimen surface after compression at 600 °C (the direction of the compression axis is vertical).

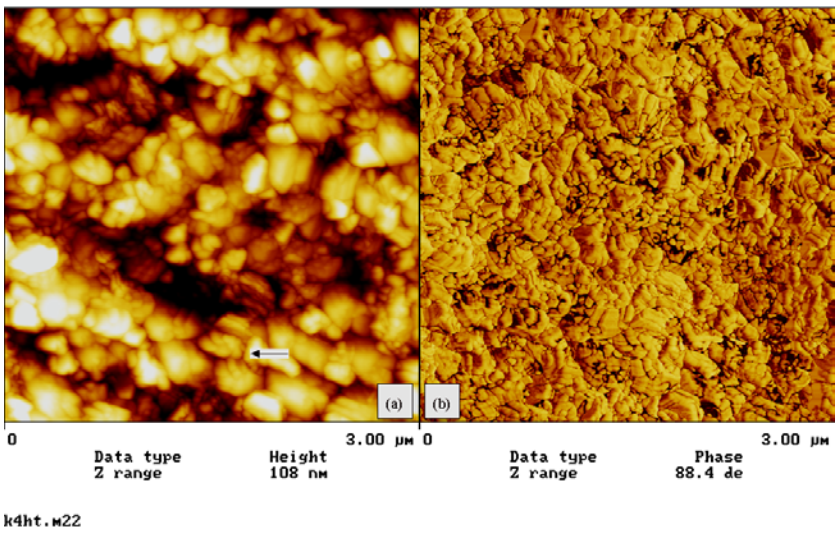

Figure 11. AFM images with high magnification (image size 3 μm × 3 μm) of the lateral specimen surface after compression at 600 °C: (*a*) height image and (*b*) phase image (the direction of the compression axis is vertical).

observations with OM indicated that a large number of macroscopic BLTs were produced by deformation (figure 7(*b*)), and they were further illustrated by AFM to be composed of a great number of sharp, long and fairly straight nanochannels (or grooves) (figure 9(*a*)). Since most of the nanochannels have the characteristics of running through in between the grains (with no clear deformation being resolved within the nanograins), this means that deformation mainly occurred in GB regions. This result suggested that some kind of GB dislocation activity or/and GB sliding were responsible for the plastic deformation. According to dislocation theory [31], the critical shear stress for dislocation generation (multiplication) is $\tau \approx Gb/L$ (here G is shear modulus, b is the Burgers vector and L the spacing between the points at which the dislocation

segment is locked). On the other hand, tensile or compressive stress σ is associated with shear stress by the relation $\sigma = m\tau$ (here m is an orientation factor having a value of 3.06 for a polycrystalline aggregate [32]). Hence, one has the relation

$$\sigma = m\tau = 3.06\frac{Gb}{L}. \tag{2}$$

In an n-material, the length of a dislocation should be constrained by its grain size. In other words, there is a relation $L \approx d$ (here d is the grain size). As a simple evaluation, substituting $b = 0.25$ nm for Ni [33], $G = 78$ GPa [29] and $d = 35$ nm into formula (2), one obtains $\sigma = 1.7$ GPa. This value coincides well with the yield stress of n-Ni–Fe at low (below room) temperatures (see figure 6). This suggests that multiplication of the dislocations with length of grain sizes could occur in n-Ni–Fe. Hence, GB dislocation activity could provide an explanation of the experimental results.

On the other hand, the SRSE $m = 0.01$ obtained at room temperature implied that one can exclude the mechanism of conventional grain boundary sliding (CGBS) at room or lower temperatures, for the value of SRSE is near 0.5 or stress sensitivity $n = 1/m = \sim 2$ for CGBS, which is more than one order higher than SRSE obtained here at room temperature. However, recently Hahn *et al* [34] proposed a new model for the deformation of n-materials based on GB migration-controlled sliding and formation of mesoscopic glide planes, in which macroscopic sliding can be realized through formation of planar interfaces by GB migration. By comparing the ultra-fine structures of the BLTs (figure 9(*a*)) with their model [34], one found that the nanochannels were extremely similar to the proposed mesoscopic planar interfaces with a slight difference that the observed nanochannels are not a strictly smooth line (planar), more or less rounding grains as they ran. This difference implies that localized sliding can proceed through some localized elastic deformation near GB regions, and large-scale GB sliding can occur without need of formation of perfectly planar interfaces. In this sliding process, the necessary stress would be much smaller than that required for dislocation activity. In other words, the present results can be explained with this new model. It is worthwhile to note that the fact that the observed plastic deformation mainly occurred in GB regions was consistent with recent theoretic simulations in n-Cu and n-Ni by molecular dynamics [35, 36], which showed that the main deformation is accommodated in GBs, or the main deformation mode is sliding in the GBs through a large number of uncorrelated events, with little dislocation activity being seen in grain interiors.

4.2. Deformation mechanism at high temperatures

Whether the deformation mechanism at low temperatures was GB dislocation activity or migration-controlled GB sliding, the gradual decrease of yield stress with temperature for $T < 200\,^{\circ}$C can be reasonably explained by thermal activation. However, as temperature was raised from 100 to 500 °C, the yield stress decreased from ∼1.6 to ∼0.15 GPa. This catastrophic decrease could hardly be accounted for by enhancement of thermal activation, particularly in view of its rapid decay character. Neither can it be attributed to grain growth, since no substantial grain growth was found after the compression test (comparing figures 2 and 9 with figure 11). Therefore, the drastic decrease in yield stress must symbolize the activation of another deformation mechanism. At high temperatures, plastic deformation can be realized through CGBS or/and diffusion creep [37]. Considering the fact that the highest temperature (600 °C) used in the tests was near $0.5T_m$, where T_m is the melting point (∼1725 K [29]) of Ni–19Fe, the CGBS through boundary diffusion was more likely to occur than diffusion creep [38].

The phenomenological equation for CGBS controlled by GB diffusion is as follows [38]:

$$\dot{\varepsilon} = A_b \left(\frac{\sigma}{E}\right)^2 \frac{D_b b}{d^3} \tag{3}$$

with the GB diffusion coefficient

$$D_b = D_{b0} \exp(-Q_b/RT) \tag{4}$$

where D_{b0} is the pre-exponential factor, Q_b the activation energy, A_b a constant ($\sim 10^8$), σ the applied stress, E the Young's modulus, R the gas constant and T the absolute temperature. Equation (3) suggests that CGBS in n-materials ($d \sim$ nm) become much more significant than in their polycrystalline counterparts ($d \sim \mu$m). Specially, the activation energy Q_b for GB diffusion in n-materials is expected to reduce remarkably, as found in ultra-fine-grained Cu ($\sim$0.2 μm) ($Q_b = 73$ kJ mol^{-1}) [17] and in nano-Cu ($Q_b = 66$ kJ mol^{-1}) [39], which were over 30% lower than that (107 kJ mol^{-1}) in coarse-grained Cu [40]. Clearly, a lower value of Q_b would lead to a rapid rise of D_b, and so a prompt decrease (or increase in $\dot{\varepsilon}$ for constant stress) in strength (for constant strain rate) on elevating temperatures. According to formula (3), the temperature behaviour of the material (yield) strength is determined by that of D_b if CGBS dominates the deformation process, since the other parameters in formula (3) are constants or weak functions of temperature. Substituting formula (4) into (3) and re-arranging it, one obtains

$$\ln \sigma = \left(\frac{Q_b}{2R}\right) \frac{1}{T} + C \tag{5}$$

where C ($=1/2 \ln(A_b b D_{b0}/(E^2 d^3 \dot{\varepsilon}))$ is a constant in the case of constant strain rate. Formula (5) indicates that $\ln \sigma$ is proportional to $1/T$ at constant strain rate. Figure 12 shows the plot of $\ln \sigma_{0.2}$ versus $1/T$ for the data taken from figure 6 as $T > 473$ K (200 °C). It can be seen that a good linear relationship between $\ln \sigma_{0.2}$ and $1/T$ existed, suggesting that deformation of n-Ni–Fe at $T > 473$ K was truly dominated by CGBS. With the best fit to the data, one obtains $C = 7.19$, and $Q_b/2R = 3796$ (K). The latter leads to $Q_b = 63$ kJ mol^{-1} (0.65 eV). This value of activation energy, similar to those in nano-Cu [40], is open for discussion.

The above analytic result suggests that at high temperatures CGBS dominated the deformation process, which can lead to occurrence of superplastic deformation. To testify to this deduction, a compression test with much larger strain was performed at 600 °C for n-Ni–Fe (figure 13). Experiments indicated that no cracking occurred in the strain range (>50%) investigated, truly demonstrating superplastic-like behaviour. In fact, CGBS was also reflected by its deformation morphology. Homogeneous deformation at high temperatures as shown in figure 10 was quite different from the case at low temperatures (figures 8 and 9). Especially, AFM revealed that after deformation a great number of grains aligned, and especially some nanograins arranged locally in twisted states (figure 11). This phenomenon indicates adjustment and displacement of grain positions during deformation, and could be considered as direct evidence of CGBS. Furthermore, it is generally believed that [41] CGBS is necessary to develop stress concentrations of the magnitude necessary for cavity nucleation. Therefore, the formation of a large number of microcavities during deformation at high temperatures (figures 10 and 11) can be considered as indirect evidence of CGBS. Hence, the characteristic temperature $T_c = \sim 340$ °C ($\approx 0.36 T_m$) (figure 6) can be considered as a sign of the deformation mechanism transition. The present result agrees well with the results reported by others [42, 43], where CGBS was found to occur at homologous temperature (T/T_m)$\sim$0.36 for n-Ni [42], and at $T/T_m = \sim 0.33$ for n-Mg [43].

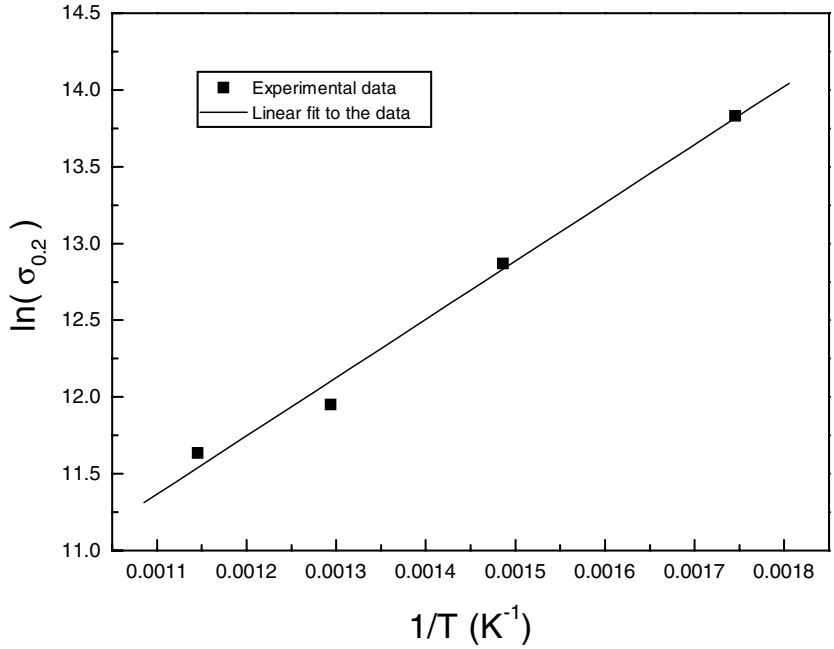

Figure 12. Plot of $\ln \sigma_{0.2}$ versus $1/T$ for the data obtained at $T > 473$ K (200 °C). The solid squares are experimental data, and the solid line is the linear fit to the data.

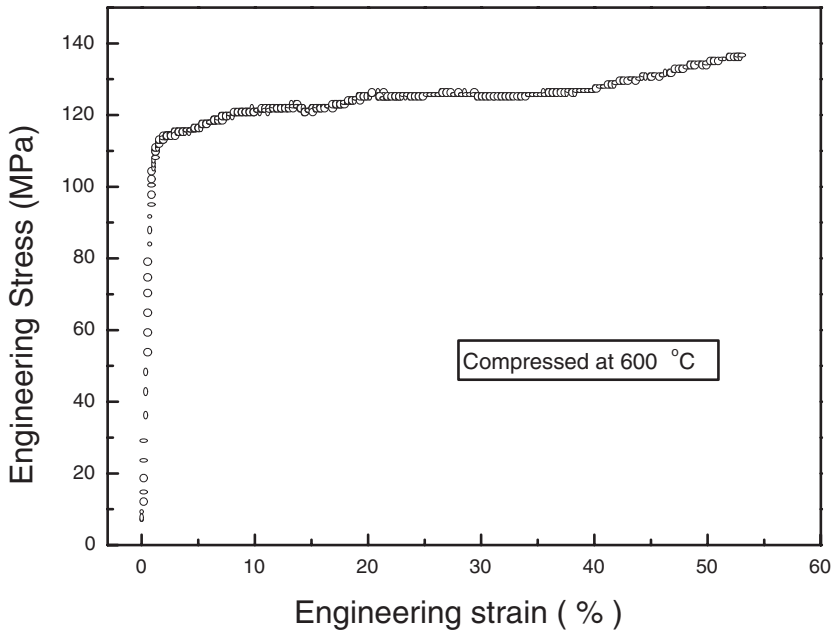

Figure 13. Engineering stress–strain curve compressed at 600 °C to the strain >50% at strain rate 1.39×10^{-4} s^{-1}.

5. Summary and conclusions

The mechanical and deformation behaviour of bulk n-Ni–19Fe (grain size $d = \sim 35$ nm) was investigated by compression and deformation trace observations in the temperature range from -162 to 600 °C. The results indicated that yield stress increased with increasing strain rate with SRSE $m = 0.01$ at ambient temperature. Yield strength ($\sigma_{0.2}$) decreased gradually with increasing temperature at temperatures $T < 100\,^{\circ}$C or $T > 400\,^{\circ}$C; while it dropped catastrophically with temperature in the temperature range $100\,^{\circ}\text{C} < T < 400\,^{\circ}$C. Deformation morphology at low temperatures was characterized by two sets of macroscopic BLTs which oriented at $\sim 55^{\circ}$ to the compression axis and consisted of sharp nanochannels running mainly through in between nanograins; high-temperature deformation led to microcavity formation, accompanying which a large number of nanograins aligned regularly, with some of them arranging locally in twisted states. Low-temperature deformation can be explained by GB dislocation activity and/or the new GB sliding model by Hahn *et al*, while high-temperature deformation would be controlled by CGBS with a transition temperature locating at $T_c \sim 340\,^{\circ}$C.

Acknowledgments

One of the authors (XYQ) gratefully acknowledges the Alexander von Humboldt Foundation for providing a fellowship so as to fulfill this work. He specially wishes to acknowledge Professor E Nembach, who, as a host professor, contributed much in both arranging all the necessary facilities available for this work and instructing the author in carrying out this research. The authors would like to thank Institut für Metallforschung, Universität Münster, for providing all the necessary facilities. In addition, the authors are indebted to Mr T Krol and Mr E Langmaack for their assistance in mechanical tests and Bodycote IMT GmbH, Essen, Germany, for HIPing experiments. This work was supported partly by the 'Hundred person programme' of Academic Sinica.

References

[1] Gleiter H 1989 *Prog. Mater. Sci.* **33** 223
[2] Suryanarayanan C 1995 *Int. Met. Rev.* **40** 41
[3] Gertsman V Y, Birringer R, Valiev R Z and Gleiter H 1994 *Scr. Metall. Mater.* **30** 229
[4] Karch J, Birringer R and Gleiter H 1987 *Nature* **330** 556
[5] Nieman G W, Weertman J R and Siegel R W 1989 *Scr. Metall. Mater.* **23** 2013
[6] Jang J S C and Koch C C 1990 *Scr. Metall. Mater.* **24** 1599
[7] Ganapathi S K and Rigney D A 1990 *Scr. Metall. Mater.* **24** 1675
[8] Höfler H J and Averback R S 1990 *Scr. Metall. Mater.* **24** 2401
[9] Qin X Y, Wu X J and Zhang L D 1995 *Nanostruct. Mater.* **5** 101
[10] Chokshi A H, Rosen A, Karch J and Gleiter H 1989 *Scr. Metall. Mater.* **23** 1679
[11] Lu K, Wei W D and Wang J T 1990 *Scr. Metall. Mater.* **24** 2319
[12] Christman T and Jain M 1991 *Scr. Metall. Mater.* **25** 767
[13] Fougere G E, Weertman J R, Siegel R W and Kim S 1992 *Scr. Metall. Mater.* **26** 1879
[14] Cheung C, Djuanda F, Erb U and Palumbo G 1995 *Nanostruct. Mater.* **5** 513
[15] Weertman J R, Niedzielka M and Youngdahl C 1993 *Mechanical Properties and Deformation Behavior of Materials having Ultra-Fine Microstructures* ed M Nastasi, D M Parkin and H Gleiter (Dordrecht: Kluwer) p 241
[16] Sanders P G, Eastman J A and Weertman J R 1997 *Acta Mater.* **45** 4019
[17] Valiev R Z, Kozlov E V, Invanov Yu F, Lian J, Nazarov A A and Baudelet B 1994 *Acta Metall. Mater.* **42** 2467
[18] Malow T R and Koch C C 1998 *Metall. Mater. Trans.* A **29** 2285
Malow T R, Koch C C, Miraglia P Q and Murty K L 1998 *Mater. Sci. Eng.* A **252** 36

[19] Nieman G W, Weertman J R and Siegel R W 1991 *J. Mater. Res.* **6** 1012
[20] Nieman G W, Weertman J R and Siegel R W 1990 *Scr. Metall. Mater.* **24** 145
[21] Wohlfarth E P (ed) 1980 *Ferromagnetic Materials* vol 2 (Amsterdam: North-Holland) p 123
[22] Kuhrt C and Schultz L 1993 *J. Appl. Phys.* **73** 1975
[23] Ge F D, Chen L M, Ku W J and Zhu J 1997 *Nanostruct. Mater.* **8** 703
[24] Eroglu S, Zhang S C and Messing G L 1996 *J. Mater. Res.* **11** 1231
[25] Zhou Y H, Harmelin M and Bigot J 1989 *Scr. Metall.* **23** 1391
[26] Qin X Y, Lee J S, Nam J G and Kim B S 1999 *Nanostruct. Mater.* **11** 383
[27] Helle A S, Easterling K E and Ashby M F 1985 *Acta Metall.* **33** 2163
[28] Lee J S, Kim T H, Yu J H and Chung S W 1997 *Nanostruct. Mater.* **9** 153
[29] Wohlfarth E P (ed) 1980 *Ferromagnetic Materials* vol 2 (Amsterdam: North-Holland) p 128
[30] Wiliam D and Callister J R 1991 *Materials Science and Engineering* 2nd edn (New York: Wiley) p 112
[31] Friedel J 1964 *Dislocations* (Oxford: Pergamon) ch 8
[32] Honeycombe R W K 1984 *The Plastic Deformation of Metals* 2nd edn (London: Arnold) p 227
[33] Friedel J 1964 *Dislocations* (Oxford: Pergamon) appendix B
[34] Hahn H, Mondal P and Padmanabhan K A 1997 *Nanostruct. Mater.* **9** 603
Hahn H, Mondal P and Padmanabhan K A 1997 *Phil. Mag.* B **76** 559
[35] Schiotz J, Vegge T, Di Tolla F D and Jacobsen K W 1999 *Phys. Rev.* B **60** 11 971
[36] Van Swygenhoven H, Spaczer M and Caro A 1999 *Acta. Mater.* **47** 3117
[37] Cahn R W, Haasen P and Kramer E J 1993 *Materials Science and Technology* vol 6, ed H Mughrabi (Weinheim: VCH) ch 9
[38] Sherby O D and Wadsworth J 1989 *Prog. Mater. Sci.* **33** 169
[39] Harvath J, Birringer R and Gleiter H 1987 *Solid State Commun.* **62** 319
[40] Kaur I, Gust W and Kosma L 1989 *Handbook of Grain and Interface Boundary Diffusion Data* vol 1 (Stuttgart: Ziegler)
[41] Cahn R W, Haasen P and Kramer E J 1993 *Materials Science and Technology* vol 6, ed H Mughrabi (Weinheim: VCH) p 434
[42] Trusov L I, Khvostantseva T P, Solov'ev V A and Mel'nikov V A 1994 *Nanostruct. Mater.* **4** 803
[43] Hwang S, Nishimura C and McCormick P G 2001 *Scr. Metall.* **44** 1507